Journal of
Ceramic Science
and Technology

J. Ceram. Sci. Technol., **12** [1] 29-36 (2021)
DOI: 10.4416/JCST2020-00026
available online at: http://www.ceramic-science.com

Effect of X (X = Al^{3+}, V^{3+}, Sc^{3+}, In^{3+} and Y^{3+}) Doping on the Dielectric Properties of Lead-Free BZT Ceramics

Zhang Kaituo[1], Xu Yuan[*1, 2, 3], Fu Lei[3], Chen Ligui[3], Jia Shikui[3]

[1]College of Cable Engineering, Henan Institute of Technology, Xinxiang 453003, China
[2]College of Materials Science and Engineering, Huaqiao University, Xiamen, 361021, China
[3]School of Material Science and Engineering, Shaanxi University of Technology, Hanzhong 723003, China
received October 15, 2020; received in revised form February 16, 2021; accepted February 28, 2021

Abstract

Al^{3+}-, V^{3+}-, Sc^{3+}-, In^{3+}- and Y^{3+}-ion-doped lead-free X-$BaZr_{0.15}Ti_{0.85}O_3$(X-BZT-15) ceramics were prepared with the solid-phase reaction method. The crystal structure, micromorphology, and dielectric properties of the X-BZT-15 ceramics were studied. X-ray diffractometry shows that the prepared ceramics have a perovskite structure. Raman spectroscopy shows that the doped ions of BZT-15 ceramics do not significantly change the vibration frequency of the $A_1(LO_3)$ mode, but have a greater impact on the new A_{1g} mode. The unit cell volume first increases and then decreases as the ion radius increases. When the doped ion radius is less than 0.0885 nm (Sc^{3+}), the substitution type of the doped cation is B-substitution. When the doping ion radius is greater than 0.0885 nm (Sc^{3+}), the substitution type of the doped cations gradually changes from B-site substitution to A-site substitution. Electron scanning microscopy shows that the doping of Y^{3+} and V^{3+} can promote grain growth, and the doping of Sc^{3+} can refine the grains. The doping of Y^{3+} can promote polarization, the doping of V^{3+} can passivate the grain boundaries, and the doping of both ions can promote the improvement of dielectric properties. The diffuseness of the phase transition shows that as the ionic radius increases, the γ value increases. The doped ions are Sc^{3+}, and the maximum value of γ is 1.877. Then γ decreases as the ion radius increases.

Keywords: Doped ionic radius, BZT, Curie-Weiss law, dielectric

I. Introduction

Perovskite material is a crystalline material with ABO_3 structure. Owing to its complex spatial structure, it has more physical properties. $BaTiO_3$ (BTO) is a typical perovskite material. It is often used in multilayer ceramic capacitors (MLCC), sensors, and memories mainly because of its lead-free properties and its outstanding dielectric, piezoelectric, and ferroelectric properties [1–3]. However, BTO ceramics are often modified for better application in device manufacturing. The Curie temperature of unmodified BTO ceramic is 120 °C. The Curie temperature can be reduced to room temperature by adjusting the doping concentrations of Sr^{+4}, Zr^{+4} and Sn^{+4} [4–7]. In addition, the dielectric constant of pure BTO ceramics is usually in the range of 1 000 to 3 000, and the dielectric properties can be improved by means of structural design, optimization and improvement of manufacturing processes. The modification of using Zr^{+4} to replace Ti^{+4} in BTO ceramics is more common in existing research. The main reason is that Zr^{+4} and Ti^{+4} have similar ionic radii and the substitution type of Zr^{+4} introduced into the crystal lattice is B-site substitution. Zr^{+4} and Ti^{+4} belong to the same main group in the periodic table, and the radius of Zr^{+4} is also larger. Therefore, the Zr^{+4} enters the position of Ti^{+4} in the barium titanate ceramic, and the chemical structure is more stable. In addition, BTO ceramics have three phase transition points of -90, 5 and 120 °C, and the three phase transition points move closer to each other as the Zr^{+4} ion content increases [8–11]. The three phase transition points coincide with each other when the Zr^{+4} ion content is 15 %. The coincidence of the three phase transitions is conducive to increasing the dielectric constant of the ceramic.

$BaZr_xTi_{1-x}O_3$ (BZT) ceramics with a Zr^{+4} ion content of 15 % are conducive to the improvement of dielectric properties and have attracted the attention of many scholars. Qitu Zhang *et al.* prepared Bi-doped $BaZr_{0.15}Ti_{0.85}O_3$ ceramics with the solid-phase reaction method, and systematically studied the effects of Bi ion doping on the dielectric properties and breakdown strength of $BaZr_{0.15}Ti_{0.85}O_3$ ceramics. The results show that the doping of Bi ions significantly reduces the dielectric loss and improves the dielectric properties [12]. Muhammad Asif Rafiq *et al.* prepared ZnO-doped $BaZr_{0.15}Ti_{0.85}O_3$ ceramics with the solid-phase reaction method, and studied the effects of different concentrations of ZnO doping in BZT ceramics based on structure, dielectric, and impedance. The results show that with the increase of ZnO concentration, the density increases and the grain size increases. Complex impedance spectroscopy revealed non-Debye type relaxation phenomenon, revealing that this relaxation of

* Corresponding author: xuyuan94@126.com

dipoles is characterized by the jumping mechanism of oxygen vacancies [13]. Wanqiang Cao *et al.* prepared Nb_2O_5 doped $BaZr_{0.15}Ti_{0.85}O_3$ ceramics with the solid-phase reaction method, and studied the effect of Nb doping on the dielectric properties of BZT ceramics. The results showed that the color of the ceramic changed from blue to yellow with the increase of the Nb_2O_5 content. The dielectric constant increases with the increase of the Nb_2O_5 doping content. When the Nb_2O_5 content is 0.10 mol%, the dielectric constant has the maximum value [14]. In addition, some reports have studied the influence of Yb, Gd, Al, Cu, Fe and other ions on the dielectric and ferroelectric properties of BZT ceramics [15–19]. All studies have the same trend that doping ions can promote grain growth and improve dielectric properties. It is worth noting that the optimal doping content is close to 1 mol%. However, the effects of doping different X-ions on the properties of $BaZr_{0.15}Ti_{0.85}O_3$ ceramics are rarely reported.

In this paper, $BaZr_{0.15}Ti_{0.85}O_3$ ceramics doped with 1 mol% of Al^{3+}, V^{3+}, Sc^{3+}, In^{3+} or Y^{3+} were prepared by means of solid-phase reaction. The crystal structure, micromorphology and dielectric properties of X-$BaZr_{0.15}Ti_{0.85}O_3$ ceramics were investigated.

II. Experimental Procedure

$BaZr_{0.15}Ti_{0.85}O_3$ ceramics doped with 1 mol% of Al^{3+}, V^{3+}, Sc^{3+}, In^{3+} or Y^{3+} (denoted X-BZT-15, where X = Al, V, Sc, In or Y) were prepared by means of solid-phase reaction. The raw materials used are $BaCO_3$ (99.8 %), TiO_2 (99.5 %), ZrO_2 (99.99 %), Al_2O_3 (99.99 %), V_2O_5 (99.99 %), Sc_2O_3 (99.99 %), In_2O_3 (99.99 %) and Y_2O_3 (99.99 %). Firstly, the raw materials were put into a nylon ball mill tank and ball-milled for 24 h according to the molar ratio. They were then dried in an oven at 120 °C. The sample material was then calcined at 1 150 °C for 12 h in a crucible. 1 mol% of oxide was weighed and ball-milled together with the above powder for 12 h. A green material having a diameter of $\varphi = 10$ mm and a thickness of $d = 1$ mm was prepared under a pressure of 20 MPa, with 5 % PVA as a binder. The ceramic green body was rapidly heated to 600 °C in a high-temperature box-type resistance furnace and held for 0.5 h so that the PVA glue could be discharged from the sample. Finally, the sample material was prepared by holding at 1 350 °C for 2 h. The samples were polished on both sides with silver paste and annealed at 600 °C for 15 min to complete the electrode fabrication.

An X-ray diffractometer was used to analyze the crystal structure of the samples. The X-ray diffractometer device model was an Ultima IV and the test range 20 ~ 80°. The Raman spectrum was measured with the 532 nm excitation at room temperature, and the equipment model used was a LabRAM HR. The density of the sample was measured according to the Archimedes principle. The microstructure was measured by a field emission electron scanning microscope, a Japan Electronics JSM-7610F Plus. The dielectric performance was measured with a Concept 50 wide-band dielectric test system produced by the German company Navocontrol Technologies.

III. Results and Discussion

Fig. 1 shows the X-ray diffraction pattern of X-BZT-15 ceramic. In the figure, all ceramic samples have a perovskite structure, which proves that the cations enter the crystal lattice well. It can be seen from the enlarged image near 45 ° that the sample doped with Sc^{3+} has a pseudo-cubic phase structure. In the figure, the diffraction peaks are chaotic with the doping of different ions, but this is not the case. The doped ions Al^{3+}, V^{3+}, Sc^{3+}, In^{3+}, and Y^{3+} have ionic radii of 0.0657, 0.078, 0.0885, 0.094, and 0.104 nm, respectively. As the ion radius increases, the diffraction peak shifts to a lower angle when the doped ion radius is smaller than the Sc^{3+} ion radius. As the ion radius increases, the diffraction peak will move to a high angle when the doped ion radius is larger than the Sc^{3+} ion radius. Al^{3+} has the smallest ion radius of all the doped ions used. The ion radius of the doped ions gradually increases from 0.0657 nm Al^{3+} ions to 0.0885 nm Sc^{3+}, so the diffraction peak moves to a small angle. The ionic radius of the doped ions in this range is B-site substitution [20–21]. When the ion radius of the doped ions is larger than Sc^{3+} and continues to increase, it is interesting that the diffraction peak appears to move to a high angle. It may be that when the ion radius is greater than 0.0885 nm (greater than the Sc ion radius), this will cause partial A-site substitution [22–23]. The A-site substitution in BZT-15 ceramics gradually increases with the increase of the doped ion radius.

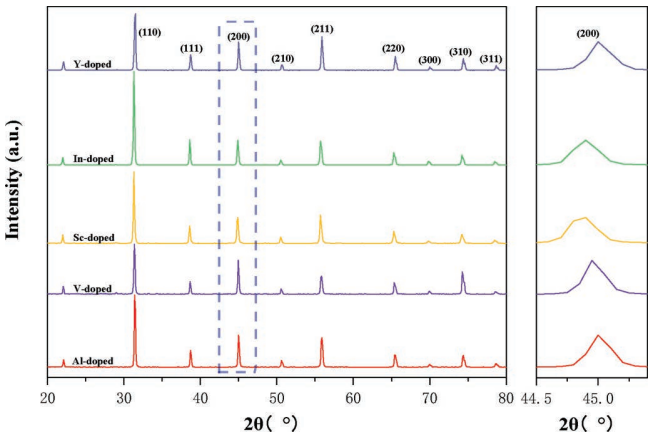

Fig. 1: XRD patterns of x-BZT-15 ceramic samples and magnification of (200) diffraction peaks.

Fig. 2 shows the volume change and density curve of the unit cell doped with different ions. In the figure, the cell volume increases as the ionic radius increases. The unit cell volume reaches its maximum when the doped ion radius increases to 0.0885 nm (Sc^{3+} ion radius). The unit cell volume decreases slowly when the doped ions are 0.094 nm (In^{3+} ion radius). When the doped ion radius is 0.104 nm (Y^{3+} ion radius), the unit cell volume drops abruptly. This may be because there is a threshold value of doped ion radius in BZT ceramics and the threshold value is near 0.0885 nm. The cell volume increases with the increase of the doped ion radius and the substitution type is B-site substitution when the ion radius of the doping element is less than the threshold value. When the ion radius of the doping element is greater than the threshold value, the cell

volume of sample decreases as the ion radius of the doped ion increases. Doped ions begin to appear as partial A-site substitutions and the number of A-site substitutions increases with increasing ionic radius. This is the same as the X-ray diffraction pattern in Fig. 1. It can be clearly seen in the figure that doped V^{3+} and doped Y^{3+} have a larger density compared to other samples, while doping Sc^{3+} and doping In^{3+} are not conducive to the increase in sample density. The change of sample density is related to the type of doped ions, but we think the main reason may be the influence of doped ions on the morphology of crystal grains. Later, we will observe the microstructure by means of SEM to further analyze the density of the sample.

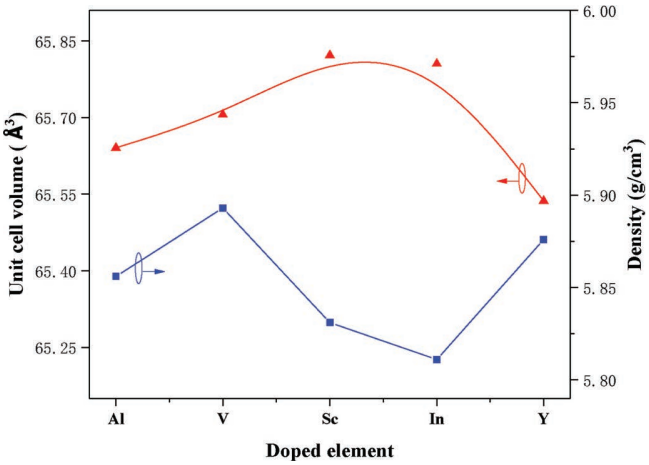

Fig. 2: x-BZT-15 ceramic unit cell volume curve and density curve.

Fig. 3 shows the Raman spectrum of the X-BZT-15 ceramic sample measured at room temperature. Three bands with peak are typical in the BTO crystal structure, which are $A_1(TO_2)$ ~265, $A_1(TO_3)$ ~521 and $A_1(LO_3)$, E (LO) ~725 cm^{-1} [24–25]. The presence of characteristic peaks can be seen in the figures. In addition, the peaks B_1,E(LO+TO) near 295 ~310 cm^{-1} are related to the tetragonal-cubic phase of BZT ceramics. In addition, there is a weak peak in BZT-15 ceramics at around 850 nm when the dopant ion is Sc ion. A weak peak becomes a strong peak when the doped ion radius is greater than the Sc ion radius. Therefore, BZT ceramics doped with Sc ions may have some tetragonal phases, and the polar axis is elongated as the radius of doped ions increases [26–27]. This corresponds to the XRD pattern of Fig. 1. $A_1(TO_3)$ mode is related to the ferroelectric phase transition and the long-range order of the dipole. It can be seen from the spectrum that the doped Sc ion has the most intense Raman peak in this mode.

Fig. 4 shows the enlarged map of $A_1(LO_3)$ mode and the map of the ratio of $A_1(LO_3)/A_{1g}$. In order to better analyze the Raman spectrum, we split the spectrum and fit it. Obviously, the new mode A_{1g} appears next to the $A_1(LO_3)$ mode [28]. In the picture, the vibration frequency of the $A_1(LO_3)$ mode did not show a large change with different ion doping. It shows that the doping of ions is not sensitive to the bonding of oxygen octahedra. However, after doping with different ions, the vibration frequency of the A_{1g} mode shows a greater change. The A_{1g} vibration frequency may be related to the polarization rate. In related reports, the A_{1g} vibration frequency decreases and the polarization rate decreases [28–29]. Samples doped with Sc^{3+} may have the lowest polarizability. In addition, the ratio of relative strength of $A_1(LO_3)/A_{1g}$ is usually used as an indicator of ferroelectricity and polarization [30–31]. In the figure, the ratio of $A_1(LO_3)/A_{1g}$ relative intensity is the smallest when doped with Sc^{3+}. Therefore, the polarization and ferroelectricity of BZT ceramics doped with Sc^{3+} may be the weakest. It can also be found in the figure that the $A_1(LO_3)/A_{1g}$ ratio of doped In^{3+} and doped Y^{3+} is the largest, indicating that the polarization and ferroelectricity may be the strongest.

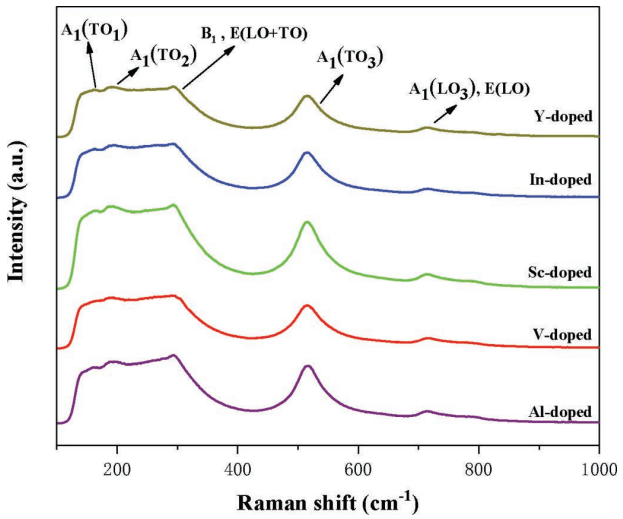

Fig. 3: Raman spectrum of x-BZT-15 ceramic measured at room temperature.

Fig. 5 (a-e) shows the scanning electron microscope photograph of X-BZT-15 ceramic. It can be seen from the photos that all ceramic samples are dense, and the grains are full and round. Fig. 5a is an Al^{3+} ion-doped BZT-15 ceramic sample. The average grain size of the sample is about 6 µm. The grains of the sample are full, and the grain boundaries are clear. Fig. 5b is a ceramic sample doped with V^{3+}. It can be seen from the figure that the grain size is large, and the average grain size is about 10 µm. In addition, it is clear in the photo that the originally angular grains are surrounded by strips. The gaps between the grains may be blurred or passivated by the strips, so that the ceramic sample is denser and corresponds to the density curve in Fig. 2. Fig. 5c shows a photo of the microstructure of the Sc^{3+}-ion-doped BZT-15 ceramic sample. It can be seen that the grain size of this sample is the smallest of all the samples, and the average grain size is only 1.5 µm. Fig. 5d shows a photo of the microstructure of the In^{3+}-ion-doped BZT-15 ceramic sample. It can be seen from the figure that the average grain size is 6 µm. In the photo, it can also be seen that the crystal grains have steep edges and are not round, which may produce some holes and reduce the density. Fig. 5e shows the Y^{3+}-ion-doped BZT-15 ceramic. It can be seen from the photo that the grains are in close contact and the grains fill the entire space, so fewer holes are generated. The average grain size of the samples is 8 µm. There are ring textures on the surface of the grains, which may be caused by the polarization of the sample.

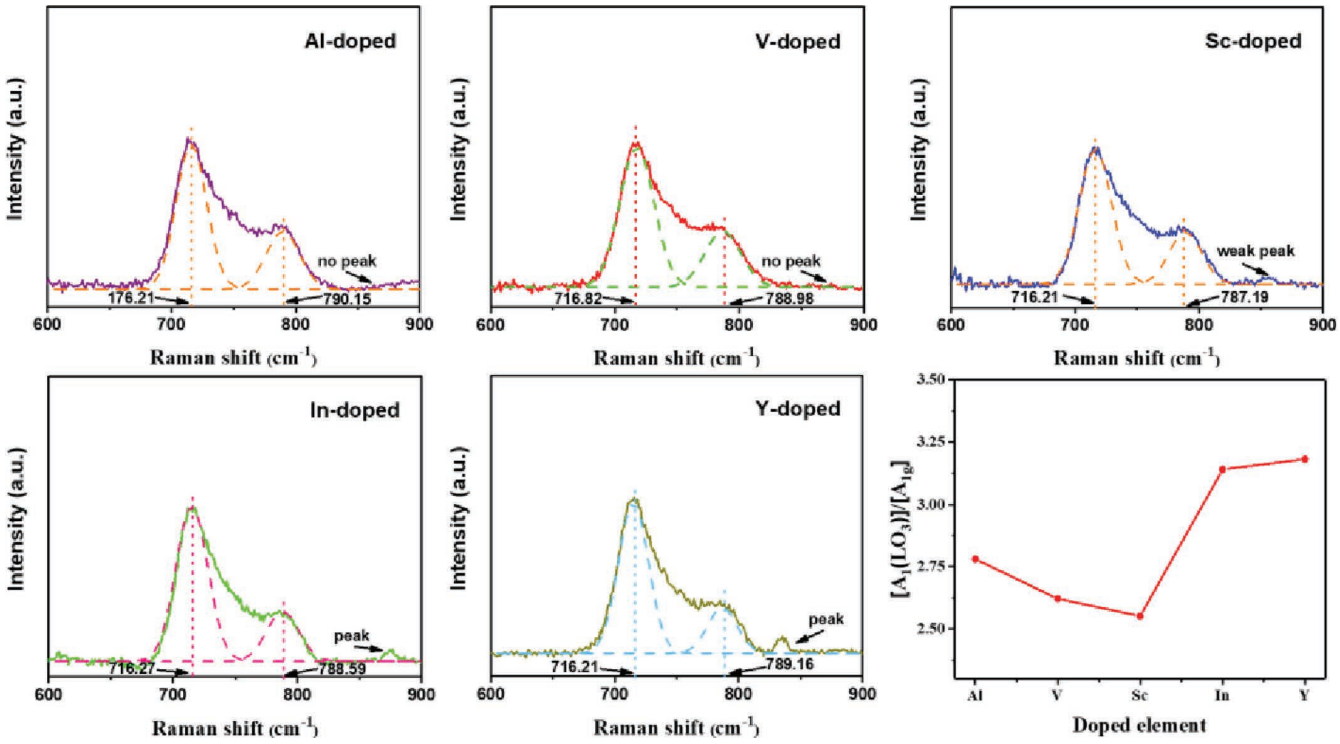

Fig. 4: The Raman spectrum of the BZT-15 sample is decomposed into A_1 (LO_3) and A_{1g} patterns and the ratio curve of A1 (LO_3) and A1 g.

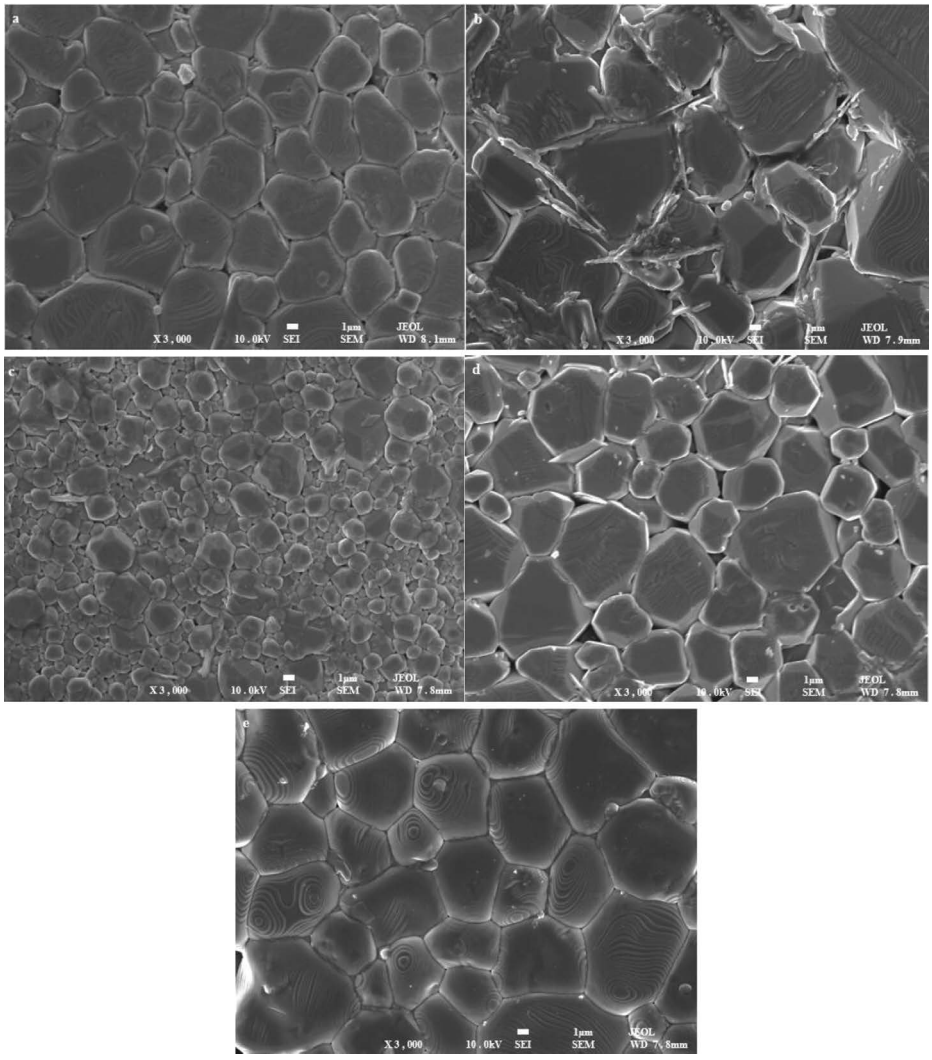

Fig. 5: SEM photos of x-BZT-15 ceramic (a) x = Al, (b) x = V, (c) x = Sc, (d) x = In, (e) x = Y.

Fig. 6 shows the dielectric constant of X-BZT-15 ceramics as a function of temperature measured at 1 kHz. In the figure, BZT-15 doped with Y^{3+} and V^{3+} has the largest dielectric constant of all the ceramic samples. These two doped samples have the same characteristics to increase the dielectric constant. The average grain sizes of BZT-15 ceramics doped with Y^{3+} and V^{3+} are 8 and 10 μm, respectively. The grain size is larger in all samples. Large-grained samples have fewer grain boundaries in the same volume. More amorphous substances at the grain boundaries in the sample are not conducive to improving the dielectric properties [32–34]. Secondly, it can be seen from the density curve that the BZT-15 ceramic samples doped with Y^{3+} and V^{3+} have a higher density, which is more consistent with the density curve shown in Fig. 2. The increase in density is beneficial to improving the dielectric properties [35–36]. These same reasons can increase the dielectric properties of the sample. The difference is that the ring-shaped texture can be seen in Y^{3+}-ion-doped samples, which may be caused by sample polarization. The sample polarization is beneficial to improve the dielectric properties of the sample. V-BZT-15 ceramics can be seen to be surrounded by strips around the grains. The presence of the strips may have the effect of passivating grain boundary defects and improve the dielectric properties of the sample.

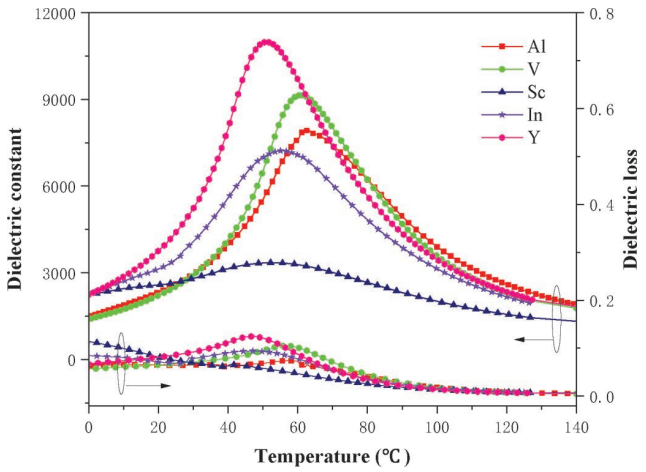

Fig. 6: Temperature dependence of dielectric constant and loss of x-BZT-15 ceramic.

It can also be seen from the dielectric temperature spectrum that as the ionic radius increases, the Curie temperature gradually decreases, and the ion radius of the doped sample increases from 0.068 nm for Al^{3+} to 0.104 nm for Y^{3+} and its Curie temperature decreases about 13 °C. First, the Curie temperature is related to the ion radius. The oxygen octahedron is deformed or distorted due to the change of doped ions. In the BZT ceramic system, the slope of the oxygen octahedron has a greater effect on the Curie temperature [37–38]. In addition, the grain size of the sample also has a certain effect. The Sc^{3+} ion radius of Sc-BZT-15 ceramic sample is 0.0885 nm, which is between the V^{3+} ion and In^{3+} ion radius. The Curie temperature should be lower than that of V-BZT-15 and larger than that of In-BZT-15. However, the Curie temperature is slightly lower than that of the In-BZT-15 sample. The grain size of Sc-BZT-15 ceramics was sharply reduced after being doped with Sc^{3+}. Similar reports have reported that the phase transition temperature of ceramic samples is reduced when the grain size is reduced [39–40].

Modified Curie-Weiss law fitting was used to analyze the relaxation of different cation-doped samples. The modified Curie-Weiss law formula is described as follows [41–42]:

$$\frac{1}{\varepsilon} - \frac{1}{\varepsilon_{max}} = \frac{(T - T_C)^{\gamma}}{C}$$

where ε is the permittivity, and ε_{max} is the maximum permittivity in a variable temperature environment. T is the temperature in a variable temperature environment. T_c is the temperature at the maximum dielectric constant. C is a modified Curie-Weiss constant and γ is a dispersion constant. When $\gamma = 1$, the sample is a normal ferroelectric, and when $\gamma = 2$, the sample is a relaxor ferroelectric. The value of γ can be drawn from the relationship between $\ln(1/\varepsilon - 1/\varepsilon_{max})$ and $\ln(T - T_c)$. Fig. 7 shows that the γ value of the doped Al^{3+} is 1.569, and the γ value increases gradually as the ion radius of the doped cation increases. When the ion radius reaches 0.0885 nm (Sc^{3+} ion), the value of γ is 1.877 to the maximum value, which is more consistent with the Raman spectrum reported. As the ionic radius continues to increase, the γ value gradually decreases, and when the ionic radius increases to 0.104 nm (Y^{3+}), the γ value decreases to 1.676. The doped ion radius can adjust the transition of BZT ceramics from standard ferroelectrics to relaxation ferroelectrics. In addition, the unit cell parameters of the sample have a certain relationship with the relaxation phase transition. When the ion radius of the doped ions is 0.0885 nm (that is, Sc^{3+}), the unit cell volume reaches the maximum, so the γ is the largest.

Fig. 8 shows the curve of the dielectric constant of the X-BZT-15 ceramic sample as a function of frequency measured at room temperature. It can be clearly seen from the figure that Y-BZT-15 ceramic has the largest dielectric constant. The first reason may be that Y^{3+} has a certain promoting effect on the increase of the dielectric constant of the ceramic, which has been analyzed above. The second reason is the effect of the Curie temperature on the dielectric constant. The test of X-BZT-15 ceramic is measured at room temperature, and the Curie temperature of BZT-15 ceramic doped with Y^{3+} is closest to room temperature. The Tc of In-BZT-15 ceramic is slightly larger than the Tc of Y-BZT-15 ceramic, so the dielectric constant is slightly lower than that of the Y-BZT-15 ceramic sample. The dielectric constant of Y-BZT-15 ceramics is greatly affected by frequency, while other samples are less affected by frequency. This is because in the dielectric frequency spectrum, the interface polarization in the low frequency region plays a dominant role [22, 26]. The Y-BZT-15 ceramic sample fluctuates greatly in this frequency range, which may be caused by a large interfacial polarization. Interfacial polarization in polarization is mainly caused by some macroscopic polarizations, such as the interface between grain boundaries, phase boundaries, and domain boundaries. Y^{3+} generates more A-site substitutions in the crystal structure, which distort the unit cell. More distortion may cause internal stress in the crystal and promote the formation of interfacial polarization. Secondly, the ring-shaped fringes produced by the crystal may also be related to interfacial polarization.

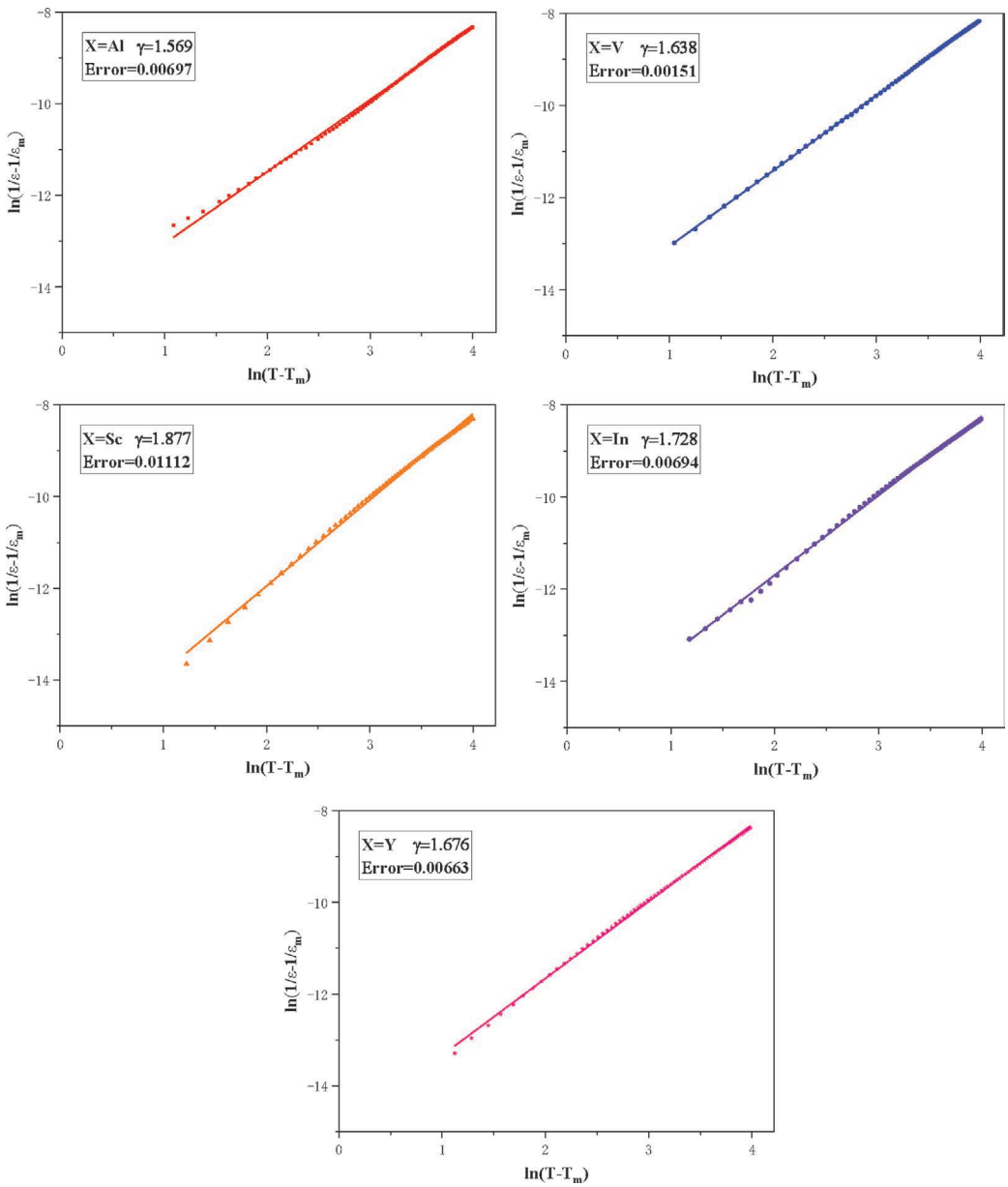

Fig. 7: Plot of $\ln(1/\varepsilon–1/\varepsilon_m)$ as a function of $\ln(T\text{-}T_m)$ of x-BZT-15 ceramics at 1 kHz.

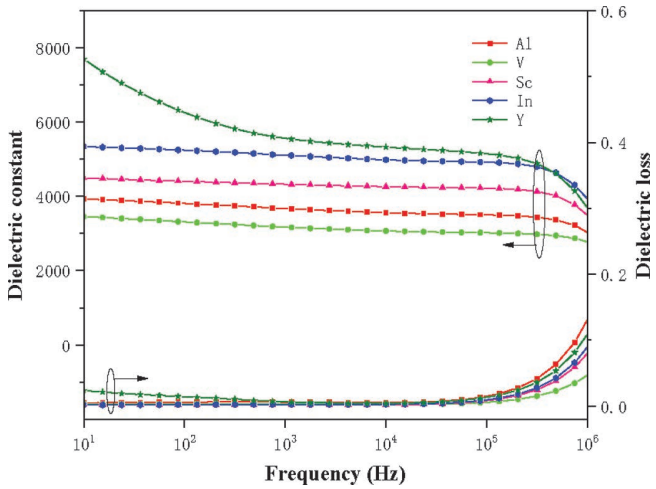

Fig. 8: Frequency dependence of dielectric constant and loss of x-BZT-15 ceramic samples measured at room temperature.

IV. Conclusions

X-BZT-15 ceramics (x = Al^{3+}, V^{3+}, Sc^{3+}, In^{3+}, Y^{3+}) were prepared with the solid-phase reaction method. Sc^{3+} with an ion radius of 0.0885 nm can be used as a limit. When the doped ion radius is below 0.0885 nm (Sc^{3+}), the X-BZT-15 ceramic sample will be replaced at the B site. The X-BZT-15 ceramic sample will be replaced at the A site when the doped ion radius is above 0.0885 nm (Sc^{3+}). The doping of Y^{3+} and V^{3+} can promote crystal growth and greatly improve the dielectric properties of ceramic samples. The relaxation phase transition of the BZT-15 ceramic sample increases with the increase of the ion radius. The γ reaches a maximum value when the radius of the doped ions is 0.0885 nm (Sc^{3+}) and then the γ is reduced. The Curie temperature moves toward lower temperatures with increasing ionic radius. The doped ion radius increased from 0.068 nm(Al^{3+}) to 0.104 nm(Y^{3+}), and the Curie temperature decreased by 13 °C.

Acknowledgements

This work was supported by National Natural Science Foundation of China (Grant No. 51703121)

Conflict of interest

The authors declared that they have no conflicts of interest with regard to this work.

We declare that we do not have any commercial or associative interest that represents a conflict of interest in connection with the work submitted.

References

1 Scott, J.F.: Applications of modern ferroelectrics, *Science*, **315**, 954 – 959, (2007).

2 Li, Y., Moon, K.S., Wong, C.P.: Electronics without lead, *Science*, **308**, 1419 – 1420, (2005).

3 Hennings, D., Schnell, A., Simon, G.: Diffuse ferroelectric phase transitions in Ba $(Ti_{1-y}\ Zr_y)O_3$ ceramics, *J. Am. Ceram. Soc.*, **65**, 539 – 544, (2010).

4 Haeni, J.H., Irvin, P., Chang, W.: Room-temperature ferroelectricity in strained $SrTiO_3$, *Nature*, **430**, 758 – 761, (2004).

5 Haertling, G.H.: Ferroelectric Ceramics: history and technology, *J. Am. Ceram. Soc*, **82**, 797 – 818, (1999).

6 Novak, N., Weyland, F., Rossetti, G.A. Jr.: Electrocaloric properties and caloric figure of merit in the ferroelectric solid solution $BaZrO_3$-$BaTiO_3$ (BZT) *J. Eur. Ceram. Soc.*, **41**, 1280 – 1287, (2020).

7 Chang, W.K, Hsieh, S.F., Lee, Y.H.: X-ray diffraction studies of phase transformations between tetragonal and cubic phases in the $BaSn_xTi_{1-x}O_3$ system, *J. Mater. Sci.*, **33**, 1765 – 1768, (1998).

8 Co, K., Khassaf, H., Alpay, S.P.: Electrocaloric and pyroelectric properties of barium zirconate titanate, *J. Appl. Phys.*, **127**, [17], 174102, (2020).

9 Xu, L., Xu, Y.: Effect of Zr^{4+} content on crystal structure, micromorphology, ferroelectric and dielectric properties of $Ba(Zr_xTi_{1-x})O_3$ ceramics, *J. Mater. Sci.: Mater. Electron.*, **31**, 5492 – 5498, (2020).

10 Sun, Z., Pu, Y., Dong, Z. *et al.*: Effect of zr $^{4+}$, content on the T_C, range and dielectric and ferroelectric properties of $BaZr_xTi_{1-x}O_3$, ceramics prepared by microwave sintering, *Ceram. Int.*, **40**, 3589 – 3594, (2014).

11 Wang, Y., Gao, S., Wang, T. *et al.*: Structure, dielectric properties of novel Ba(Zr,Ti)O 3 based ceramics for energy storage application, *Ceram. Int.*, **46**, 12080 – 12087, (2020).

12 Zhang, Y., Li, Y., Zhu, H. *et al.*: Low dielectric loss of Bi-doped $BaZr_{0.15}Ti_{0.85}O_3$, ceramics for high-voltage capacitor application, *Ceram. Int.*, S0272884217312877 (2017).

13 Muhammad, Q.K., Waqar, M., Rafiq M.A.*et al.*: Structural, dielectric, and impedance study of ZnO-doped barium zirconium titanate (BZT) ceramics. *J. Mater. Sci.*, **51**, 10048 – 10058 (2016).

14 Cao, W., Xiong, J., Sun, J.: Dielectric behavior of Nb-doped $BaZr_xTi_{(1-x)}O_3$, *Mater. Chem. Phys*., 106, 338 – 342, (2007).

15 Li, Y., Cui, Z., Sang, R.*et al.*: Microstructure and dielectric behavior of ytterbium doped $BaZr_{0.1}Ti_{0.9}O_3$ ceramics, *Mat. Res.*, **19**, 1376 – 1380, (2016).

16 Xi, K., Li, Y., Zheng, Z. *et al.*: Microstructure, dielectric properties, relaxation behavior, and ferroelectric properties of Gd-doped lead-free BZT ceramics by sol-gel process, *J. Mater. Sci.: Mater. Electron.*, [8], 1 – 8, (2020).

17 Feng, H., Ji, H., Li, X.*et al.*: Effect of Al_2O_3 and MgO additives on dielectric properties of $BaZr_xTi_{1-x}O_3$-based ceramics, *Key Eng. Mater.*, 2 – 603:714 – 718 (2014).

18 Sun, Z., Li, L., Zheng, H. *et al.*: Dielectric properties and diffuse phase transition behavior of CuO-doped lead-free $Ba(Zr_xTi_{1-x})O_3$ ceramics, *Ceram. Int.*, 12246 – 12252 (2016).

19 Yan, S., Zheng, Z., Li, Y.*et al.*: Effect of internal stresses on temperature-dependent dielectric properties of Fe-doped BZT ceramics, *Ceram. Int.*, 12605 – 12608, (2017).

20 Khien, N.V., Huy, T.T., Hong, L.V.: AC conduction of $Ba_{1-x}Ca_xTiO_3$ and BZT-BCT_x, *Physica B.*, **532**, 126 – 129 (2017).

21 Tian, Y., Li, S., Sun, S.*et al.*: Influence of europium doping on various electrical properties of low-temperature sintered $0.5Ba_{0.90}Ca_{0.10}TiO_3$-$0.5BaTi_{0.88}Zr_{0.12}O_3$-0.1%CuOxEu lead-free Ceramics[J], *J. Electron Mater.*, 684 – 691 (2018).

22 Kumar, R., Asokan, K., Patnaik, S. *et al.*: Evolution of relaxor properties in lanthanum (La) doped barium zirconate titanate, *Ferroelectrics*, 8 – 13, (2017).

23 Ghosh, S.K., Ganguly, M., Rout, S.K. *et al.*: Order-disorder correlation on local structure and photo-electrical properties of La^{3+} ion modified BZT ceramics, *Eur. Phys. J. Plus*, **130**, 68, (2015).

24 Lu, D.Y., Sun, X.Y., Liu, B. *et al.*: Structural and dielectric properties, electron paramagnetic resonance, and defect chemistry of Pr-doped $BaTiO_3$ ceramics, *J. Alloy. Compd.*, **615**, 25 – 34. (2014).

25 Liu, S., Xie, Q. *et al.*: Tunable electrocaloric and energy storage behavior in the ce, mn hybrid doped $BaTiO_3$ ceramics, *J. Eur. Ceram. Soc.*, **38**, S0955221918303820, (2018).

26 Lu, D.Y.: Self-adjustable site occupations between Ba-site Tb3+ and Ti-site Tb4+ ions in terbium-doped barium titanate ceramics, *Solid State Ion.*, **276**, 98 – 106, (2015).

27 Ji, B., Chen, D., Jiao, X. *et al.*: Preparation and electrical properties of nanoporous $BaTiO_3$, *Mater. Lett.*, **64**, 1836 – 1838, (2010).

28 Sun, Z., Liu, W., Li, Q. *et al.*: Relaxor behaviour and nonlinear dielectric properties of lead-free BZT-BZN composite ceramics, *Ceram. Int.*, **47**, 2086 – 2093, (2021).

29 Buscaglia, V., Saurabh, T. *et al.*: Average and local atomic-scale structure in $BaZr_xTi_{1-x}O_3$ (x = 0.10, 0.20, 0.40) ceramics by high-energy x-ray diffraction and raman spectroscopy, *J. Phys. Condens. Matter*, (2014).

30 Ventura, J., Hernández, S., Polo, M.C. *et al.*: Discrimination of polar order extent in $BaZr_xTi_{1-x}O_3$ epitaxial thin films by raman spectroscopy, *Appl. Surf. Sci.*, 424374 – 377, (2017).

31 Pokorny, J., Pasha, U.M., Ben, L., Thakur, O.P., Sinclair, D.C., Reaney, I.M.: Use of raman spectroscopy to determine the site occupancy of dopants in $BaTiO_3$, *J. Appl. Phys.*, **109**, 114110, (2011).

32 Zheng, P., Zhang, J.L., Tan, Y.Q. *et al.*: Grain-size effects on dielectric and piezoelectric properties of poled $BaTiO_3$ ceramics, *Acta Mater.*, **60**, 5022 – 503, (2012).

33 Guo, F.Q., Zhang, B.H., Fan, Z.X. *et al.*: Grain size effects on piezoelectric properties of $BaTiO_3$ ceramics prepared by spark plasma sintering, *J. Mater. Sci.: Mater. Electron.*, **27**, 5967 – 5971, (2016).

34 Wang, J.C., Zheng, P., Yin, R.Q. *et al.*: Different piezoelectric grain size effects in $BaTiO_3$ ceramics, *Ceram. Int.*, **41**, 14165 – 14171, (2015).

35 Tian, X., Qu, S., Ma, H. *et al.*: Effect of grain size on dielectric and piezoelectric properties of bismuth layer structure $CaBi_2Nb_2O_9$ ceramics, *J. Mater. Sci.: Mater. Electron.*, **27**, 1 – 5 (2016).

36 Tseng, C.F., Tseng, P.J., Chang, C.M. *et al.*: Novel temperature stable Li_2MnO_3 dielectric ceramics with high Q for LTCC applications, *J. Am. Ceram. Soc.*, **6**, 1918 – 1922 (2014).

[37] Xu, Y., Zhang, K., Fu, L. *et al.*: Effect of MgO addition on sintering temperature, crystal structure, dielectric and ferroelectric properties of lead-free BZT ceramics, *J. Mater. Sci: Mater. Electron.*, **30**, 7582 – 7589, (2019).

[38] Abassi, M., Dhahri, N., Dhahri, J. *et al.*: Structural and large magnetocaloric properties of $La_{0.67-x}Y_xBa_{0.23}Ca_{0.1}MnO_3$ perovskites ($0 \leq x \leq 0.15$)($0 \leq x \leq 0.15$), *Physica B: Condensed Matter,* 138 – 143, (2014).

[39] Reddy, S.B., Rao, M.S.R., Rao, K.P.: Observation of high permittivity in Ho substituted $BaZr_{0.1}Ti_{0.9}O_3$ ceramic. *Appl. Phys. Lett.*, **91**, 022917 – 022917, (2007).

[40] Polotai, A.V., Ragulya, A.V., Randall, C.A.: Preparation and size effect in pure nanocrystalline barium titanate ceramics, *Ferroelectrics*, **288**, 93 – 102, (2003).

[41] Vandamme, L.K.J., Khalfallaoui, A., Leroy, G. *et al.*: Thermal equilibrium noise with 1/f spectrum from frequency independent dielectric losses in barium strontium titanate, *J. Appl. Phys.*, **107**, 053717 – 053717, (2010).